Surface Acoustic Waves-Localized Plasmon Interaction in Pillared Phononic Crystals

A. Noual[1,2,*] R. Akiki,[3] Y. Pennec,[3] E. H. El Boudouti,[1] and B. Djafari-Rouhani[3]

[1]*LPMR, Département de Physique, Faculté des Sciences, Université Mohamed Premier, 60000 Oujda, Morocco*

[2]*Département de Physique, Faculté Pluridisciplinaire Nador, Université Mohamed Premier, 60000 Oujda, Morocco*

[3]*IEMN, UMR CNRS 8520, Département de Physique, Université de Lille, 59655 Villeneuve d'Ascq, France*

We study numerically the interaction of surface acoustic waves propagating at the surface of a multilayer structure (the so-called Sezawa waves) with localized surface plasmons at the bottom of metallic pillars deposited on the substrate. The pillars are made of gold and the multilayer structure is constituted by a layer of gold on a silicon substrate and covered by a thin spacer of dielectric material. We are interested in localized plasmons, which are the analog of metal-dielectric-metal surface plasmons. The physical characteristics of these plasmons, such as their eigenvalues and absorption or reflection spectra, are modulated by surface acoustic waves due to deformation of the structure in the vicinity of the pillars. The surface waves are generated in the area in front of the pillars deposited on the substrate. Two types of acoustic modes are envisioned to interact with the localized plasmons, namely, confined modes associated with the local resonances of the pillars and the propagating Sezawa modes that deform the structure in the vicinity of the surface. We discuss the efficiency of phonon-plasmon coupling for both types of modes and select those that can be useful for an experimental realization based on this platform. Also, we show that, besides the plasmon frequency, the phonon-plasmon coupling magnitude strength is sensitive to the distance between the pillars, which reveals the role of interactions between the pillars on the coupling. The geometrical parameters are chosen such that the acoustic waves are in the sub-GHz range and the plasmons are around the telecommunication wavelength of 1.55 μm. This work may help with the design of optomechanical devices that can be controlled by fast coherent acoustics and facilitate applications involving enhanced sound-light interactions, such as light modulation.

I. INTRODUCTION

Lately, a great deal of attention has been paid to the interaction of ultrahigh-frequency elastic waves with optical waves within nano- or microscale photonic structures, with a view to manipulating or modulating the optical properties of the latter [1–5]. Such devices are termed as optomechanical structures, and the intense interest they raise is related to their utility in both fundamental physics for controlling mechanical motion by light and quantum information processing and their potential practical applications as sensors for high-precision measurements of mass, charge, or small distances [5–9]. Two physical mechanisms are involved in the coupling of acoustic phonons and light inside a homogeneous bulky material: (i) the first one is due to the local stress field generated by the passage of the acoustic wave, known as the photoelastic effect [10,11]; and (ii) the second mechanism is

based on perturbation by the elastic waves of the structural interfaces of the system, which is called the interface moving effect [12]. To achieve strong optomechanical interactions, certain types of nano- and microstructures have been used lately, the so-called phoxonic crystals [13]. These structures can exhibit simultaneous band gaps for both photons and phonons, that is, they can support both light and sound localization within the same cavity, giving rise to enhanced photon-phonon coupling. Based on these crystal cavities, optomechanical (OM) interactions have been greatly investigated in two-dimensional (2D) crystals [14,15], nanobeams [16–21], and crystal slabs [22–25]. More recently, Aram and Khorasani studied optomechanical coupling strength in various triangularly shaped phoxonic crystal cavities [26], and Hsu *et al*. have shown efficient generation of a hybrid plasmonic-photonic band gap using acoustic Lamb waves [27]. On the other hand, phonon-plasmon coupling has been demonstrated in phoxonic-plasmonic slab cavities based on periodic metal strips [28] and through the use of acoustic surface

*noualad@yahoo.fr

waves, where strong optomechanical interactions in hybrid photonic-plasmonic crystal nanocavities have been shown [29].

Additionally, it is well established that localized surface plasmon (LSP) waves supported by small metallic nanoparticles give rise to a high degree of light confinement [30,31]. In particular, light intensity can be enhanced several orders of magnitude closer to the particle surface over a much smaller length scale than that of light wavelength in vacuum. This outstanding property has been harnessed in a number of applications, such as biosensors [32–34], photothermal therapy [35,36], and to achieve plasmon-induced enhancement of solar-cell efficiency [37, 38]. Furthermore, coupling of LSP with vibrating nanoparticles of different shapes have been intensely studied; we can cite, for instance, the work of van Dijk *et al.* [39] who studied gold spherical nanoparticles, or cubic particles [40], rods [41], columns [42], and antennas [43]. Generally, the interaction of the LSP and mechanical oscillations sustained by metallic nanoparticles are studied via pump-and-probe experiments [44,45] or based on Raman scattering [46–48]. Lately, Mrabti *et al.* [49] have studied numerically the phonon-plasmon interaction in a system made of gold nanocylinders coupled to a Au film and sitting on a Si membrane.

Let us also stress that, recently, the use of high-frequency ($\sim$GHz) surface acoustic waves (SAW) to realize coherent coupling between optical and acoustic waves [50], or for achieving coherent phonon-photon interaction in a multiple photonic nanocavity-based optomechanical platform [51], has been demonstrated. Moreover, optomechanical interactions have been shown to enable bidirectional conversion between optical and microwave photons using a pair of radially symmetric Lamb wave interdigital transducers (IDTs) coupled to an optomechanical crystal cavity [52]. However, investigations of surface plasmon interactions with phonons using SAW have rarely been reported in the literature. Yet, the experimental realization of SAW platforms is readily accessible and allows the production of high-amplitude acoustic waves for the purpose of an efficient coupling with plasmons. Indeed, nowadays, SAW can be easily generated using IDTs [53] or pulsed laser beams [54]. Additionally, the phonon-plasmon interaction occurs in a small (subwavelength) region of space, owing to the localized and high-intensity nature of the LSP, while the conception of a plasmonic cavity can be much easier than that in typical phoxonic crystals proposed and designed in the literature. Besides, phonon-plasmon coupling enables further enhanced optomechanical interactions, which could lead to important fundamental physical studies [26,29]. Not long ago, phonon-plasmon interactions were exploited for investigations into the mechanical vibrations of metallic nanoparticles [55,56] or plasmonic molecules [57]; therefore, SAW-based phonon-plasmon devices may facilitate such studies even further.

Motivated by this context, we develop an alternative approach in this paper based on the use of SAW for the investigation of phonon-localized surface-plasmon-enhanced interactions in a multilayer structure. First, we study the phononic and optical properties of a system consisting of a periodic array of gold nanocylinders (AuNCs) deposited on top of a multilayer structure, where the latter is made of a silicon substrate supporting an Au metal film covered by a thin polymer material, which acts as a spacer with respect to the pillars. Then, we investigate the surface waves interaction with localized plasmons at the bottom of the pillars, which are analogs of the metal-dielectric-metal LSP (MIM LSP) and are chosen to arise in the near-infrared frequency range (around $1.55\,\mu$m). The region underneath the AuNCs, where the MIM LSP is confined, acts as an effective MIM cavity. Subsequently, elastic phonons deforming this cavity volume result in the modulation of the frequency of the resonating plasmonic mode. The structure exhibits two types of surface acoustic modes, namely, localized phonons confined in the pillars and propagating Sezawa waves near the surface. The interaction of these two types of modes with localized plasmon is investigated using the moving-interface effect. We demonstrate effective modulation of the plasmon frequency by certain Sezawa and localized phonons through the simulation of the system plasmon eigenfrequency versus elastic-mode phase. We also show the role of interactions between the pillars on phonon-plasmon coupling magnitude strength. Localized and Sezawa phonons that strongly couple with the plasmon might be useful for the conception of experimentally realizable SAW devices based on the proposed platform. Such systems, which can be easily integrated on chip, may lead to various potential applications, such as ultrasensitive sensors [58] or acousto-optic modulators [59].

This paper is organized as follows: in Sec. II, we present full three-dimensional (3D) numerical simulations of the phononic properties of the periodic multilayer structure. In Sec. III, we focus on the optical properties of the system and then, in Sec. IV, we investigate Sezawa and localized phonon-plasmon coupling. In Sec. V, we study the surface acoustic waves interaction with localized plasmon exhibited by the multilayer system, where one row of gold pillars is placed on top. The conclusions are given in Sec. VI.

II. PHONONIC PROPERTIES

A sketch of the studied structure is presented in Fig. 1(a); it consists of a square array of gold nanocylinders sited on a multilayered substrate composed of a gold metal film, a thin polymer material (polyamide) acting as a spacer, and a semi-infinite substrate made of silicon lying underneath. A magnification of a unit cell of such structure is depicted in Fig. 1(b). Throughout the paper, AuNCs have a radius of $R = 165$ nm and a height of
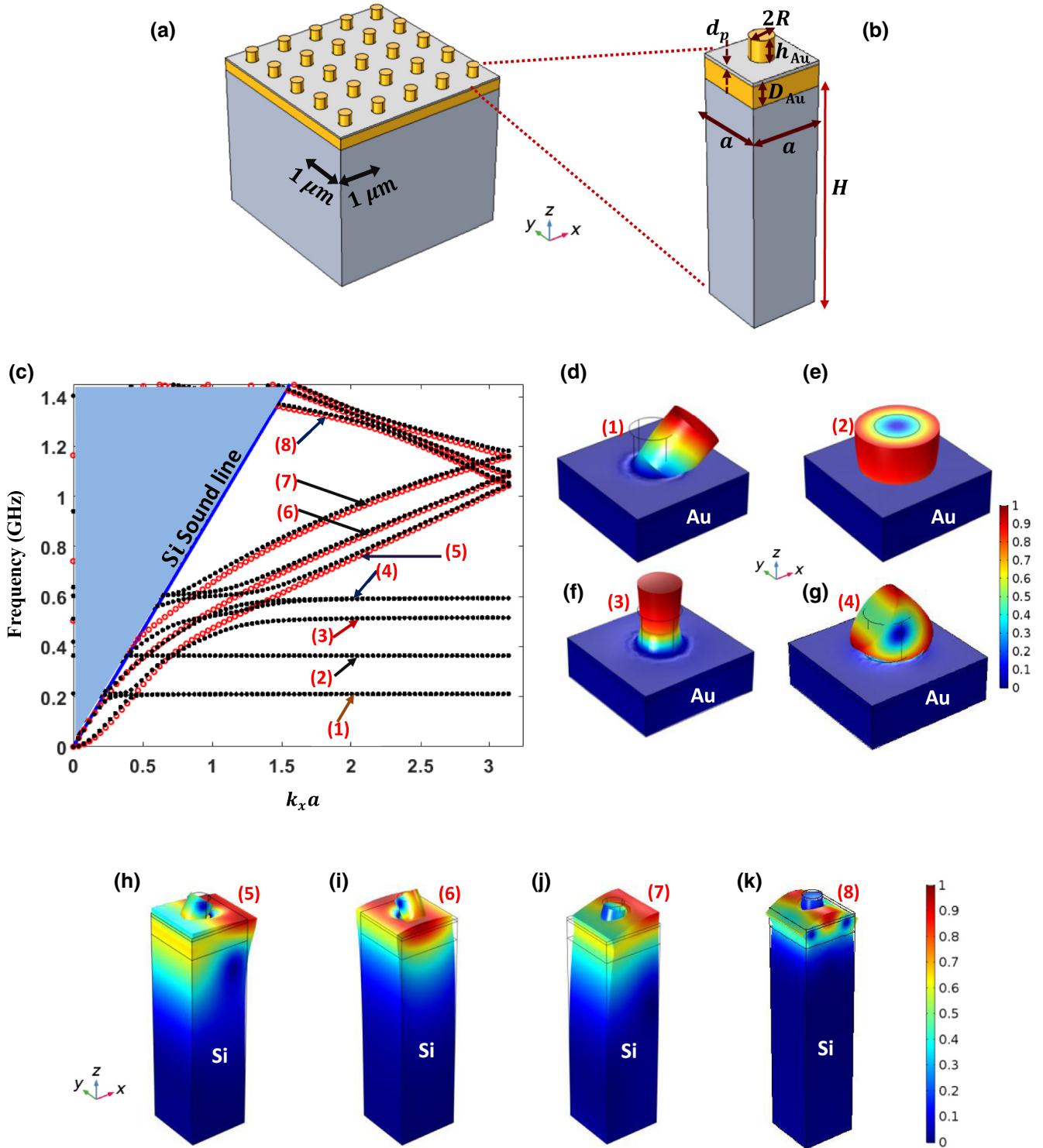
FIG. 1.   (a) Schematic diagram of the studied structure. (b) Magnification of a unit cell of the structure, indicating the shape parameters of the nanocylinder and multilayer substrate. (c) Simulated band diagram of the structure depicted in (a) in black dotted lines. Dispersion curves of the structure in absence of gold nanocylinders are also plotted in red circles. (d)–(g) Displacement field maps of the localized modes within the gold nanocylinders (the Si substrate where the field vanishes for these modes is not shown), referred to as (1)–(4) in (c), respectively. (h)–(k) Same as in (d)–(g), but for the modes referred to as (5)–(8) in (c), which are localized in the Au thick film near the surface of the device (Sezawa modes). Except for mode (8), depicted at $k_x a = 1.68$, remaining modes are all given at the same reduced wave vector, $k_x a = 2$. Presented displacement fields maps are normalized with respect to their maximum value within the system.

$h_{Au} = 300$ nm; the thickness of the polymer spacer is chosen to be $d_p = 50$ nm, whereas the Au film is $D_{Au} = 100$ nm thick and the lattice parameter is set as $a = 1000$ nm. The polymer material is an isotropic medium, the elastic properties of which are represented by a Young's modulus of $E = 2.5$ GPa, a Poisson ratio of $\nu = 0.34$, and a density of $\rho = 1400$ kg/m^3. On the other side, gold is an anisotropic material with a face-centered cubic crystal structure and silicon crystallizes in a face-centered diamond cubic structure; their elastic constant parameters, C_{11}, C_{12}, and C_{44}, were taken from Ref. [11]. Numerical simulations in this paper are performed based on the finite element method using commercial software COMSOL Multiphysics.

In particular, to get the band diagram of the structure, we use the solid mechanics module in COMSOL with the following boundary conditions: Floquet periodic conditions are applied along the x and y directions, the free surface is set on top of the system, while a low-reflection boundary is chosen at the bottom of the structure to mimic a semi-infinite substrate. Moreover, the thickness of the latter in the model is chosen to be large enough, such as $H = 10a$, to realize accurately the condition of a semi-infinite substrate. Figure 1(c) shows the simulated band diagram of the system along the $\Gamma - X$ direction. The four lower branches below the sound line in silicon are totally flat from $k_x a \geq 1.5$ onwards; these are eigenmodes of the gold nanocylinder. It is worth pointing out that the first and fourth branches are two-times degenerate modes associated with flexural motions of the pillars. Above the four branches, three other dispersive branches are apparent, resulting from the folding of the former at the Brillouin zone edge due to periodicity. These three branches arise from the interaction of Sezawa modes localized in the Au thick film and the AuNCs localized modes, giving rise to the observed dispersive curves. To show this, we plot, in small red-square markers in Fig. 1(c), the dispersion curves of the structure in the absence of AuNCs, namely, the Rayleigh-Sezawa modes. The latter reveals three branches that superimpose quite well with branches of the pillared system [Fig. 1(a)] in the mid- and high-frequency ranges. Their displacement fields (see below) indicate strong localization in the gold film underneath the surface. Figures 1(d)–1(g) present displacement field maps corresponding to the lower four eigenmodes localized in gold nanocylinders [branches (1)–(4) in Fig. 1(c)]. On the other hand, in Figs. 1(h)–1(k), we give the field maps corresponding to some of the modes originating from Sezawa branches, [identified as (5)–(8) in Fig. 1(c)]. The twofold degenerated modes (1) are a first-order flexural mode of the cylinder along the 0 - x and 0 - y axes, the frequency of which is about 0.2 GHz; mode (2) is a radial breathing mode (of the cylinder) at a frequency of about 0.35 GHz; mode (3) is a compression mode, where the cylinder gets compressed symmetrically towards its

axis at a frequency of about 0.508 GHz. The compression is accompanied by an elongation movement along the z axis. The degenerate fourth mode (4) is a higher order flexural mode with an eigenfrequency of 0.58 GHz. Displacement field maps of modes (5) (≈ 0.71 GHz), (6) (≈ 0.83 GHz), (7) (≈ 0.91 GHz), and (8) (≈ 1.33 GHz) indicate that these are Sezawa modes confined within the Au film near the surface and coupled, to some extent, with AuNC modes. Gold nanocylinders in modes (5)–(7) are entrained in a flexural-like motion [Figs. 1(h)–1(j), respectively] and in a compression-elongationlike motion in mode (8) [Fig. 1(k)]. We are particularly interested in those eigenmodes that have a fraction of the associated elastic energy localized within or around the dielectric spacer, that is, inside the volume where the MIM LSP mode of the system shall be localized. This will result in their overlapping, and hence, possibly their coupling. In order to check how the elastic energy of modes (1)–(8) is distributed inside the structure (except in the substrate where the field vanishes for these modes), especially within the dielectric spacer, we plot in Figs. S1(a)–S1(h) within the Supplemental Material [60] the rate of the elastic strain energy density localization in a z-x cut plane of the structure. The former is defined as the ratio of the elastic strain energy density integrated over the spacer volume reported to the maximum value taken by the energy density within the volume of the whole structure, that is,

$$E_{loc} = \frac{\iiint_{V_{spacer}} U dv}{\text{Max}_{V_{tot}}(U)}, \qquad (1)$$

where U is the strain energy density; it reads for an elastic anisotropic material as follows:

$$U = \frac{1}{2} C_{ijkl} \varepsilon_{ij} \varepsilon_{kl}, \qquad (2)$$

where C_{ijkl} is the components of the fourth-order stiffness tensor of the material and ε_{ij} (or ε_{kl}) is the strain tensor component. From Figs. S1(a)–1(h) within the Supplemental Material [60], one can note that modes (1) and (2) show quite weak localization of the energy within the dielectric spacer, as opposed to the rest of the modes; compressional mode (3) indicates the higher localization rate (~ 30 %). Sezawa surface mode (7) shows the second highest rate of localization and is followed by Sezawa modes (8), (5), and (6), respectively. High-order flexion mode (4) manifests a comparable localization to that of mode (5). Notably, mode (8) shows some strain energy localization near the Si substrate, which simply relates to the deformation induced by this mode close to the interface of the Au film and the silicon substrate underneath. Clearly, modes (3)–(8) seem to be good candidates for the acousto-optic interaction; subsequently, it is important to get a more specific idea of how these modes might affect a resonating MIM LSP

mode within the dielectric spacer. To that end, we analyze in Figs. S1(i)–S1(t) within the Supplemental Material [60] the behavior of the real parts of the displacement field components along the x axis (component u) and along the y axis (component v), associated with modes (3)–(8) in the dielectric spacer. The volume of the spacer layer situated right underneath the gold nanocylinder acts as an effective cavity, where a propagating surface plasmon (in a MIM-like structure) reflects off the cylinder bottom edges, resulting in plasmonic standing waves. The resonance wavelengths of the latter are sensitive to the (effective) cavity thickness (which is the spacer thickness) and its length, which matches the cylinder diameter. This means that elastic modes changing one of these dimensions or both of them shall modulate the resonance-plasmon-mode wavelength. Thus, it is essential to determine how the studied modes deform the effective cavity volume during an acoustic period of time. According to Figs. S1(i)–S1(t) within the Supplemental Material [60], mode (3) significantly compresses-stretches the MIM cavity volume during an acoustic period in an isotropic manner, and, as a result, a strong coupling between the MIM LSP and mode (3) is expected. Similarly, Sezawa eigenmodes (7) and (8) stretch and compress the cavity along the x and y axes, leading to its volume deformation. Nonetheless, this deformation is not as uniform as that for mode (3), which means the coupling strength might be different from that of mode (3). In mode (4), the cavity oscillates together with the cylinder with some volume deformation occurring, especially along

the x axis; the deformation is much weaker than those of modes (3) and (8), so should be the plasmon-phonon coupling magnitude. Sezawa mode (5) stretches the cavity mainly along the x axis, resulting in a non-negligible volume deformation of the cavity and suggesting that a good phonon-plasmon interaction rate might be observed with this mode. A weak volume deformation of the effective cavity might be observed, according to u and v component maps of Sezawa mode (6); the deformation magnitude is indeed seemingly smaller (almost negligible) than those of modes (7), (8), and (5), which indicates a much lower phonon-plasmon coupling strength.

III. PLASMONIC PROPERTIES

To simulate the optical properties of the system, a medium of incidence (air) is added on top of a unit cell of the structure, as shown in Fig. 2(a). We consider a normally incident plane wave polarized such that its electric field oscillates along the 0-x axis. The wavelength domain of interest here lies at around 1550 nm [(1440 nm–1720 nm)]. The refractive index of the polymer material (polyamide) is $n_p = 1.7$, and gold metal is modeled based on the Lorentz-Drude model.

Floquet periodic boundary conditions are applied along the 0-x and 0-y axes and port boundary conditions are set on the inlet (on top) and outlet (at bottom) of the structure. Figure 2(b) gives the simulated absorbance and reflectance spectra of the structure, where an important
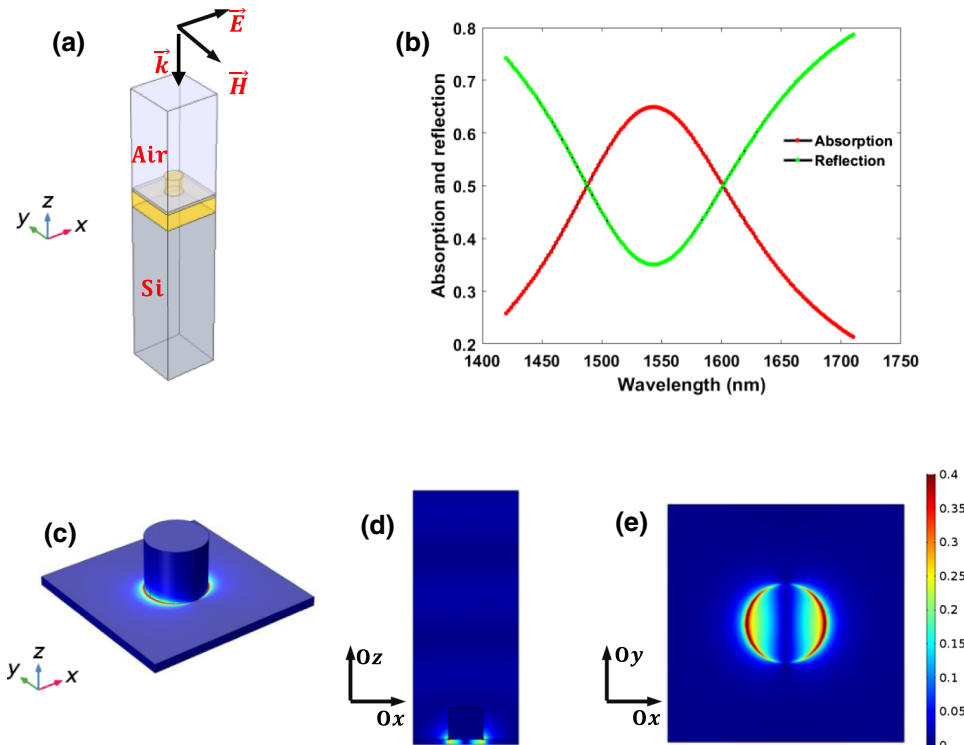
FIG. 2. (a) Sketch of a unit cell of the structure depicted in Fig. 1(a), on top of which an incidence medium made of air is added. A linearly polarized plane wave (E field along x axis) normally falling down on the structure is shown. (b) Corresponding simulated absorbance and reflectance spectra. (c) Electric-field norm map plotted within the dielectric spacer and Au nanocylinder. The E-field norm is normalized to its maximum value in the whole structure. (d),(e) Same as in (c), but in a z-x cut-plane geometry (median plane) and in the x-y plane lying right underneath the gold nanocylinder, respectively.

absorption band, extending from about 1420 to 1720 nm, occurs; it reaches its higher rate of about 65% at a wavelength of about 1543 nm. At the same time, the reflectance falls, at this same wavelength, to around 35%, indicating a strong localization of light within or around the AuNC. The associated electric-field norm distribution with the observed absorption peak is depicted within the polymer spacer and the AuNC in Fig. 2(c), where it can be seen that the light wave is trapped down at the bottom of the pillar. The E-field distribution is also shown in the median z-x plane of the structure and in the x-y plane situated right underneath the AuNC, in Figs. 2(d) and 2(e), respectively. It is apparent that the excited mode is strongly localized within the dielectric spacer at the bottom of the AuNC, fitting the description of the so-called MIM LSP in Ref. [49] fairly well. The effective cavity below the AuNCs, where the standing plasmonic waves form is called a MIM cavity hereafter. If the diameter of the gold particle is stretched to infinity, we end up with a unidimensional structure made out of silicon substrate (infinite)/Au (300 nm)/polyamide polymer (50 nm)/Au (300 nm)/air [Fig. 3(a)]. This system supports, among (several) other modes, MIM surface plasmon-polariton (MIM SPP) modes confined within the polymer spacer [49], and which propagate with wave vector k_{SPP}, as shown in the inset of Fig. 3(a). The latter is sensitive to the dielectric spacer thickness and is dependent on the incident light wavelength. We plot in Fig. 3(a) the corresponding dispersion curve along with the light line in the polymer material. Based on Fig. 3(a), the effective index of the propagating surface plasmon is $n_{\mathrm{eff}} = k_{\mathrm{SPP}}/k_0 \approx 2.4204$ for a wavelength in vacuum equal to 1543 nm (resonance wavelength of the plasmon mode observed in Fig. 2). Along the interface on which the surface plasmon propagates, the wavelength is about $\lambda_{\mathrm{SPP}} \approx (2\pi/k_{\mathrm{SPP}}) \approx 637\,\mathrm{nm} \approx 2D$, where $D = 2R$.

Hence, the MIM plasmon mode typically has a wavelength in the order of the cylinder diameter ($D = 330$ nm), which provides a convincing explanation as to why plasmonic standing waves can form in the MIM cavity. Furthermore, we depict in Fig. 3(b) the transverse E_z component of the E-field map of a propagative MIM SPP mode, along with black arrows showing E_z-field lines, and in Fig. 3(c) we give the map of the transverse component of the E-field E_z associated with the MIM LSP (with black arrows showing lines of E_z) confined to the MIM cavity. The maps show quite similar behavior of the transverse components of the electric fields in both cases, which indicates the origin of the observed plasmon mode in Fig. 2, that is, the reflection off the AuNC bottom edges of the propagating MIM SPP modes, giving rise to resonating plasmonic standing waves.

It is worthwhile noting that E_z-field arrows [Fig. 3(c)] indicate that E_z reaches its maximum near the MIM-cavity edges; on the other hand, E_z can be expressed as

$$E_z(\rho, \phi) = \cos(m\phi) J_n(k_{\mathrm{SPP}}\rho), \qquad (3)$$

where J_n is the Bessel function of first order, n ($n \in \mathbb{N}$); (ρ, ϕ) are the polar coordinates and $m \in \mathbb{N}$. Hence, the plasmonic standing waves confined in the MIM cavity should approximately verify the condition

$$\frac{\partial E_z}{\partial \rho}(\rho = R) = 0 \Rightarrow J_n'(k_{\mathrm{SPP}}R) = 0. \qquad (4)$$

If we denote by x_{mn} that the Bessel function's derivative equals zero, then the dispersion relation of the plasmonic standing waves within the MIM cavity is

$$k_{\mathrm{SPP}}(d, \lambda) = \frac{x_{mn}}{R}. \qquad (5)$$
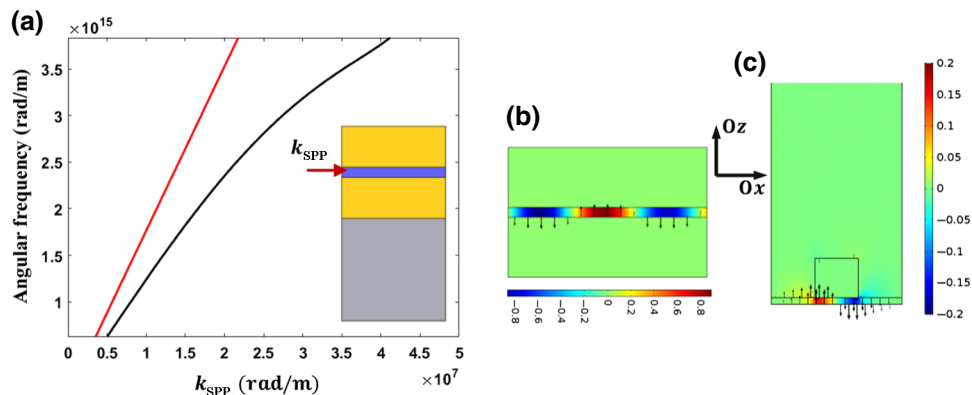
FIG. 3.   (a) Dispersion curve (black line) of a 2D MIM-waveguide system. The latter structure consists of a silicon substrate (infinite)/Au(300 nm)/polyamide polymer(50 nm)/Au(300 nm). Light in polyamide polymer material is plotted as red line. Schematic illustration of the structure is shown in the inset. (b) Transverse component, E_Z, of the electric-field map of propagative surface plasmon in the system of (a); black arrows indicating the E_Z lines are also shown. (c) Same as in (b), but for MIM LSP confined to the MIM cavity of the structure of Fig. 2(a).

Based on Fig. 3(c), the confined MIM LSP mode in the MIM cavity corresponds to the first zero of $J'_n(k_{SPP}R)$, i.e., $x_{11} \approx 1.841$, which means that $m = 1$ and $n = 1$ for this mode. It is noteworthy that, although the MIM LSP mode observed in Fig. 2 is essentially confined at the bottom of AuNCs, it still couples with localized plasmons of the neighboring AuNCs. We observe that the absorbance spectrum of the system [of Fig. 2(a)] is fairly sensitive to lattice parameter a. The corresponding result is presented in the Supplemental Material [60] (Fig. S2), where a is varied from 1000 to 1400 nm (remaining parameters are unchanged). An increase of a results in an almost linear redshift of the plasmonic mode frequency until $a \geq$ 1500 nm where the redshift saturates.

IV. PLASMON-PHONON COUPLING IN THE PERIODIC STRUCTURE

In this section, we study the effect of localized and Sezawa elastic modes (3)–(8) on the plasmonic properties of the structure in Fig. 1(a). In this regard, we use the so-called moving interface (or moving mesh) effect, which accounts for the acoustic-induced deformations along each interface (between two materials) of the system [12]. Because an acoustic period of about 10^8/s is several orders of magnitude smaller than that of an optical cycle in the order of 10^{14}/s, we use the quasi-static approximation, in which, at an instant of time of the deformed geometry, we calculate the new resonance plasmon mode frequency. Specifically, we simulate the absorbance spectrum or the optical eigenfrequency of the structure for different phases, $\varphi = 2\pi f t$, during an acoustic period, where f is the eigenfrequency of the elastic mode of interest and t is time. The deformation amplitude applied via the moving-mesh effect is assumed to be such that the maximum elastic displacement inside the nanocylinder equals 1% of its height, which yields $u_{max} = 3$ nm. This value is relatively high compared with those produced by an acoustic surface wave generated by interdigital transducers in front of the structure. Nonetheless, owing to the linear dependence of the plasmon eigenfrequency modulations with the amplitude of the acoustic deformation, we use such higher values for the sake of numerical simulations, which can be then scaled to smaller deformations. To assess the plasmon-phonon coupling magnitude, we investigate the evolution of the plasmon eigenwavelength versus the elastic phonon phase, φ. Specifically, we compute the absorption coefficient for three different values of φ to illustrate how the former can be shifted, and we simulate the plasmon eigenwavelength for a set of values $\in [0 - \pi]$.

In Figs. 4(a)–4(d), we present the absorbance spectra of the system for the values of the phase $\varphi = 0, \pi/2, \pi$ for elastic modes (3), (5), (7), and (8), while in Figs. S3(a)–S3(b) within the Supplemental Material [60] we give the absorbance spectra for modes (4) and (6) that

display a weak phonon-plasmon coupling. Clearly, for modes (3), (5), (7), and (8), the absorption coefficient undergoes an important shift because its maximum position changes with φ. Conversely, modes (4) and (6) exhibit almost no effect [see Figs. S3(a)–S3(b) within the Supplemental Material [60]], except for a very little change in the absorption spectrum shape for mode (4) between $\varphi = 0$ and $\varphi = \pi/2, \pi$, which we attribute to the degree of mesh refinement in numerical simulations. We give, in Figs. 4(e)–4(h), the simulated eigenwavelength (in vacuum) of the MIM-cavity plasmon mode as a function of φ for modes (3), (5), (7), and (8). For modes (4) and (6), the results are presented in Figs. S3(c)–S3(d) within the Supplemental Material [60]. It is worth pointing out that the simulated eigenwavelength corresponds approximately to the wavelength of the maximum in the absorption spectrum.

Notably, localized elastic mode (3) and Sezawa mode (7) induce the strongest plasmon-phonon coupling magnitudes, as the plasmon-mode frequency-maximum modulation amplitude reaches a value of $\Delta\lambda_{max} \approx 31$ nm between $\varphi = 0$ and $\varphi = \pi$ for mode (3) and $\Delta\lambda_{max} \approx$ 34 nm for mode (7) [Figs. 4(e) and 4(g), respectively]. On the other hand, the modulation amplitudes for modes (5) and (8) amount to $\Delta\lambda_{max} \approx 17$ nm [Fig. 4(f)] and 25 nm [Fig. 4(h)], respectively. The observed modulation amplitudes characterized by $\Delta\lambda_{max}$ measure the phonon-plasmon coupling strength, and we observe that, overall, they are consistent with the predictions made in Sec. II based on the analysis of the shapes of modes (3), (5), (7), and (8) and how they would deform the effective MIM cavity. Concerning modes (4) and (6), the value of $\Delta\lambda_{max}$ tends to zero [see Figs. S3(c)–S3(d) within the Supplemental Material [60]], which is in agreement with the behavior of absorbance versus φ observed in Figs. S3(a)–S3(b).

V. PLASMON-PHONON COUPLING BASED ON THE GENERATION OF SURFACE ACOUSTIC WAVES

A. Transmission based on SAW

In this section, we investigate the coupling of localized and Sezawa elastic modes of the structure with the studied plasmon mode of the MIM cavity using the generation of surface acoustic waves in front of the plasmonic structure. This is to provide proof of concept by showing numerically how the plasmon-phonon coupling with the proposed geometry design could be experimentally realized. As a first step, we focus on the analysis of the transmission properties of the system based on surface elastic waves. Figure 5(a) shows a sketch of the geometry design of the studied structure. For simplicity, we choose to set one infinitely periodic row of gold pillars roughly in the middle of the structure on top, along the y axis, namely, there is only one unit cell along the x axis. Such a configuration
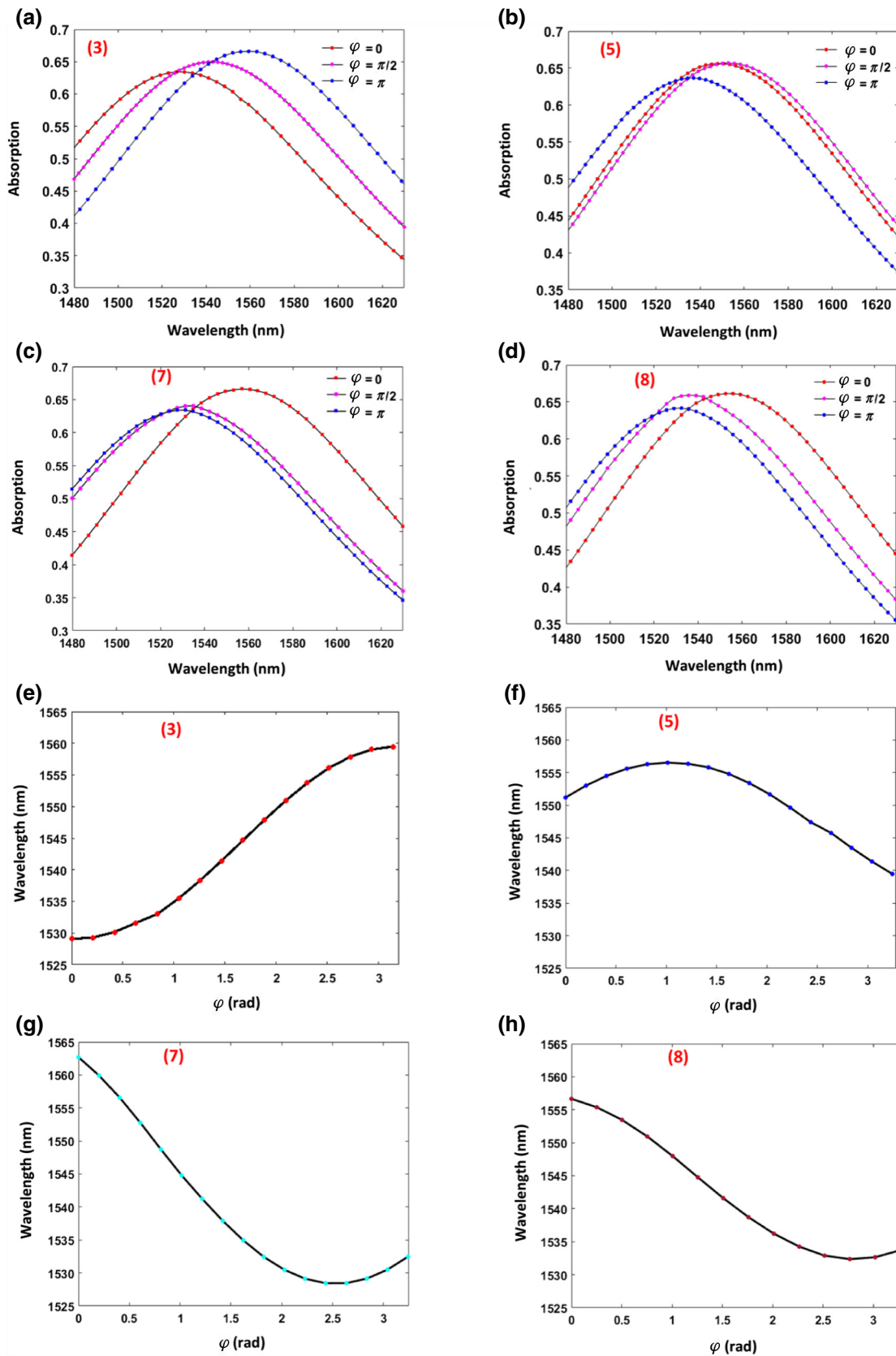
FIG. 4. (a)–(d) Absorbance spectra of the system depicted in Fig. 1(a) for three #values of phase φ of localized elastic mode (3) and Sezawa modes (5), (7), and (8) of Fig. 1. (e)–(h) Simulated eigenwavelength (in vacuum) of the plasmon mode of the MIM cavity as a function of phase φ for modes (3), (5), (7), and (8), respectively.
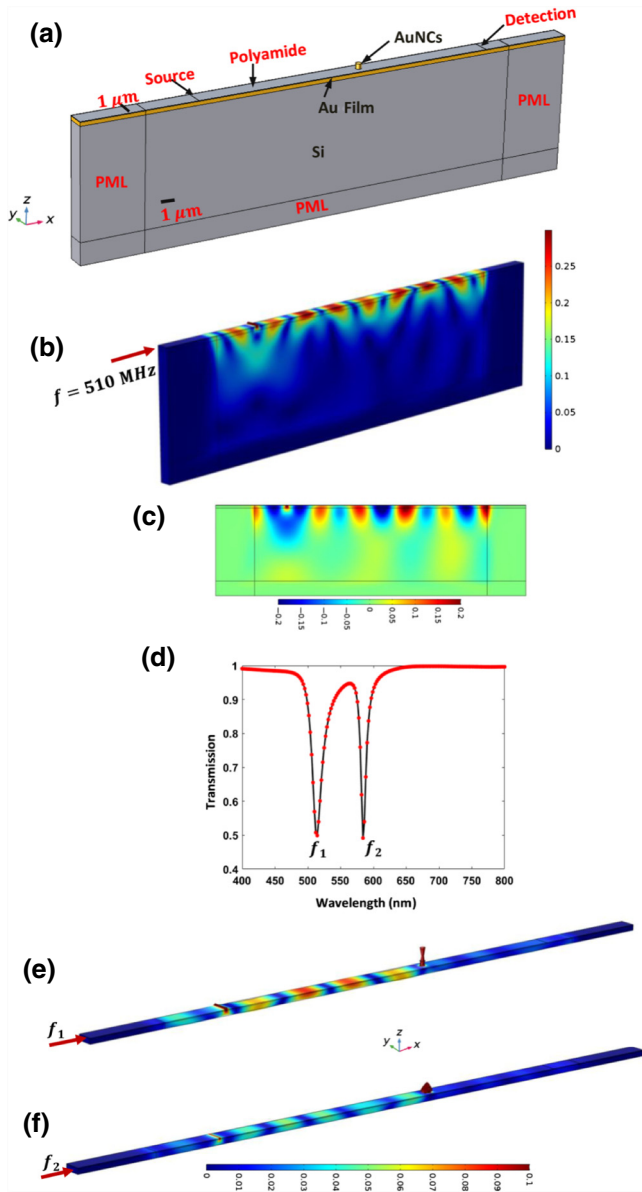
FIG. 5. (a) Schematic of the studied geometry design used for the transmission of surface elastic waves. It consists in one periodic row of AuNCs along y axis, deposited on multilayer silicon substrate, as in Fig. 1(a) and surrounded with perfectly matched layer (PML) domains, to remove undesired reflections. (b) Displacement field norm map within the structure associated with a propagating Sezawa surface wave at frequency $f = 510$ MHz. (c) Map of the w component of the displacement field in 0-x-z cut plane of the system (median plane). (d) Simulated transmission spectrum of the structure depicted in (a). (e),(f) Displacement field (norm) map at frequencies of the observed dips in (d), that is, at $f_1 \approx 513$ MHz and $f_2 \approx 584$ MHz, respectively.

is in line with the work in Ref. [61], where the scattering properties of incident Lamb waves with a single silicon pillar or a line of pillars deposited on a thin silicon plate have been investigated. The system is finite along

the propagation direction $(0 - x)$. Perfectly matched layers are placed all around the structure to get rid of undesired reflections perturbing the system. The geometrical parameters characterizing the structure, such as the gold nanocylinder height and radius, the period of the grating (along $0 - y$ axis), and the layer thicknesses of the materials, are kept unchanged, as previously discussed. To excite the system, we employ a vertical force along a line source on top of the polymer material, as shown in Fig. 5(a).

In Figure 5(b), we show the displacement field $\sqrt{|u|^2 + |v|^2 + |w|^2}$ map within the structure for an incident plane wave at a frequency of $f = 510$ MHz (this almost matches the frequency of the cylinder compression mode studied above). Figure 5(c) depicts the w component of the field within the median cut plane (0-z-x) of the system. Based on these figures, we observe the strong confinement of the propagating waves close to the multilayer surface, indicating the excitation of a Sezawa surface wave. To study the interaction of the incident surface wave with the row of AuNCs, we simulate the transmission spectrum of the structure [Fig. 5(a)]; the frequency span extends from 400 to 800 MHz, which ensures the inclusion of compressional mode (3) and degenerate flexural mode (4) of the cylinder. Figure 5(d) gives the corresponding results, where we note the excitation of two localized modes, since two dips appear in the transmission spectrum.

The dips are situated at $f_1 \approx 513$ MHz and $f_2 \approx 584$ MHz, which can be associated with compressional mode (3) of the AuNCs at 508 MHz and flexural mode (4) at 580 MHz, respectively, in Fig. 1(a). This is confirmed in Figs. 5(e)–5(f), where we present the displacement field map within the upper layers (including PMLs) of the system, for clarity, at the dip frequencies. It can be seen that the incident surface waves excite and strongly couple with compressional [Fig. 5(e)] and flexural modes [Fig. 5(f)] of the nanocylinder, resulting in the reflection of waves towards the system inlet.

As far as experimental generation of SAW is concerned, a piezoelectric material with comb-shaped arrays of electrodes may be used to electrically excite high-frequency SAWs at the inlet on top of our device. For instance, a piezoelectric thin film, such as ZnO or AlN, can be deposited on the surface [53], or else the thin film might be deposited only on the inlet and outlet of the system surface, as shown in Ref. [62], leaving the original structural design unchanged in between. Another means by which high-frequency ($\sim$GHz) SAW can be generated and detected is the employment of short pulsed lasers [54,63]. Such an approach does not require a change to the proposed multilayer system by adding piezoelectric materials. This method may operate such that a pump pulsed laser is focused on top at the inlet of the device to generate SAWs, then a probe beam is sent over the outlet surface, the deflection and diffraction of which enables the detection and analysis of the transmitted SAW [54].

B. Localized surface plasmon of the system

In this part, we briefly look at the MIM-cavity plasmon modes displayed by the system depicted in Fig. 5(a) at around 1543 nm. The latter is different from the periodic structure of Fig. 1(a) because it is composed of only one unit cell along 0-x instead of a periodic array. Subsequently, an adapted geometry for optical simulations should be set to determine the plasmonic modes of the system. Figure 6(a) presents such a geometry, where an air medium is added on top of the AuNC/Si substrate, and PML media removed because we aim to perform an eigenfrequency search (for plasmonic modes).

Numerical details concerning the optical simulations of the system are given within the Supplemental Material [60]. In Figs. 6(b) and 6(c), we give the electric-field norm map within the simulated media of the structure, where it can be observed that the excited plasmonic mode corresponds well with the MIM-cavity plasmon mode studied in Sec. III. This is particularly explicit when comparing the mode structure observed here [Fig. 6(c)] in the 0-x-y cut plane with the one seen in Fig. 2(e). The eigenwavelength (in vacuum) of the MIM-cavity plasmon mode observed here is $\lambda_{SPP} \approx 1602$ nm, which is redshifted compared with the value obtained above ($\lambda_{SPP} \approx 1543$ nm). This can be explained based on Fig. S2 within the Supplemental Material [60], where we observe that an increase of lattice parameter a or equivalently the distance between AuNC redshifts the plasmon mode frequency (revealing the role of interactions between AuNC in their optical response). Indeed, in the studied system here, there is one periodic row of AuNC on top along the y axis, which is similar

to the case where a is increased (to infinity along the x axis) in the periodic structure of Fig. 1(a). The calculations are realized, as previously discussed, at different phases, $\varphi \in [0 - \pi]$, of the acoustic surface wave.

Concerning the applied deformation, we set the value of the linear force exciting the incident surface wave so that the maximum elastic displacement within gold pillars is in the order of $u_{max} \approx 3$ nm, which is equivalent to the maximum displacement set in AuNC in the infinitely periodic system studied in Sec. IV. Specifically, the application of a linear force of $F \approx 22$ N/m yields a maximum displacement in gold pillars equal to $u_{max} \approx 2.98$ nm. Simulation results are reported in Fig. 7(a), where we can observe that the plasmonic mode wavelength is modulated by excited localized phonon via the incident surface wave, with a maximal oscillation amplitude of $\Delta\lambda_{SPP\,max} \approx 19.9$ nm. The latter value is nearly 36% smaller than the one observed in Fig. 4(e). This relates to the sensitivity of phonon-plasmon coupling magnitude to lattice parameter value a (or distance between Au pillars), reflecting the influence of interactions between Au pillars on phonon-plasmon coupling strength. Indeed, we note in Fig. 7(b), where we plot $\Delta\lambda_{SPP\,max}$ [for mode (3), plasmon coupling] versus lattice parameter a in a periodic system of Fig. 1(a), that an increase of a from 1000 to 1400 nm results in a drop of $\Delta\lambda_{SPP\,max}$ of about 27%, which is close to the $\Delta\lambda_{SPP\,max}$ drop seen in Fig. 7(a) [where depicted results correspond to the system of Fig. 5(a) for which a is infinity].

Comparable values to $\Delta\lambda_{SPP\,max3} \approx 20$ nm observed in Fig. 7(a) [mode (3)-plasmon interaction] can be achieved using another dielectric material instead of the polymer
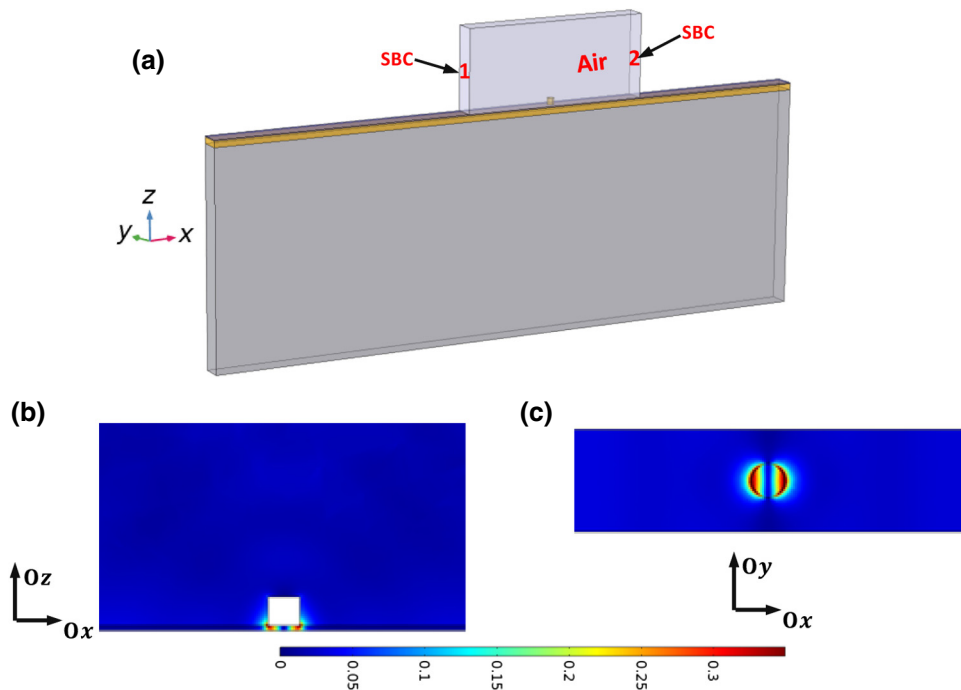
FIG. 6. (a) Sketch of the geometry platform used for phonon-plasmon coupling using incident surface elastic waves as a means of excitation of localized phonons in the gold pillars. The structure is similar to that in Fig. 5(a), except that an air medium is added on top of the gold nanocylinders for optical simulations. PMLs surrounding the system are not shown for simplicity. At facets 1 and 2, delimiting the air domain, scattering boundary conditions (SBC) are applied to prevent undesired reflections at these boundaries. (b),(c) Electric-field norm map within 2D cut planes of the system, 0-z-x and 0-x-y, respectively, in the parts of the structure where optical simulations are performed.
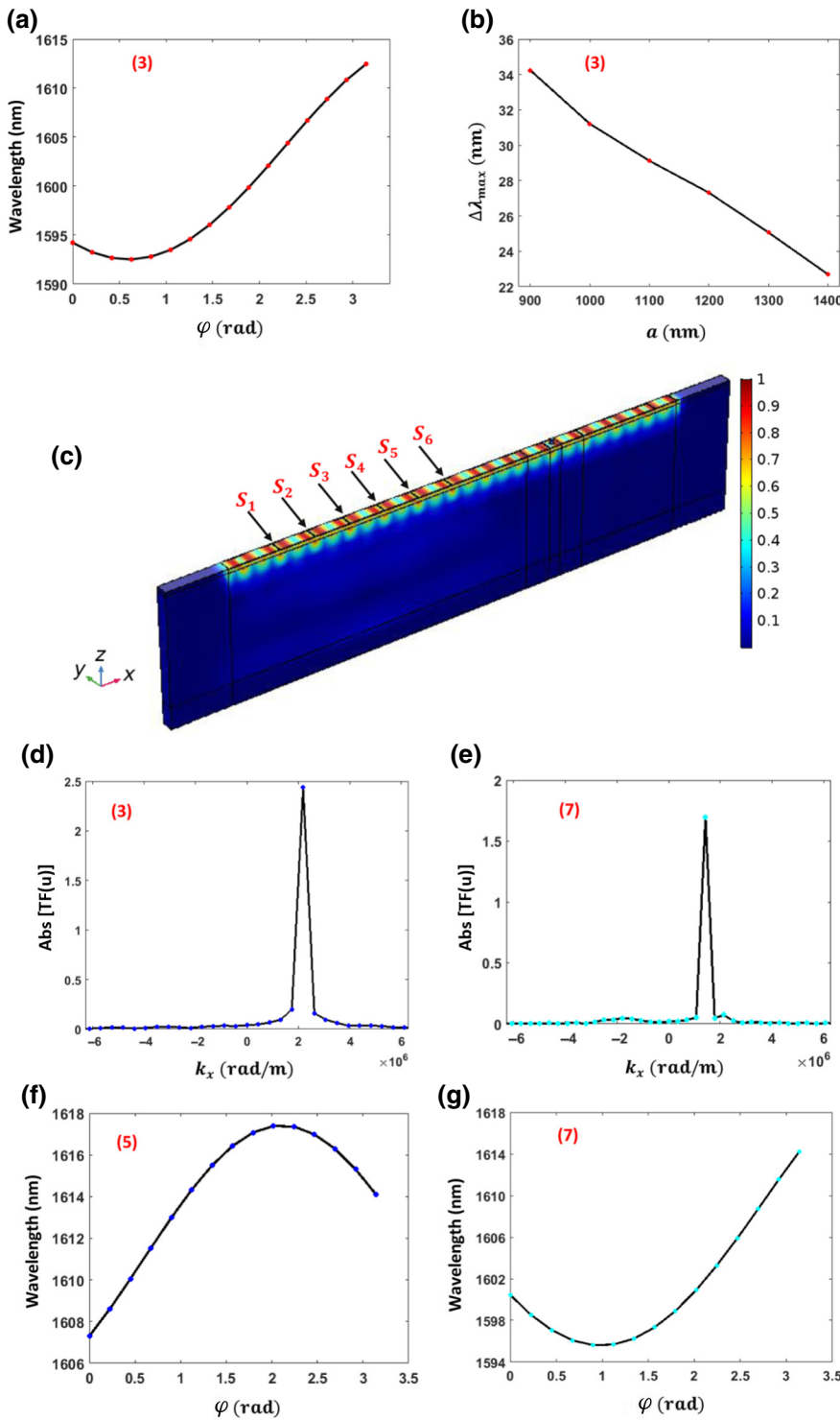
FIG. 7. (a) Plasmonic mode eigenwavelength (in vacuum) as a function of incident elastic surface wave phase $\varphi \in [0 - \pi]$. Frequency of the latter is set at $f = 510$ MHz to match that of localized mode (3). As a result, the latter mode is excited by incident SAW and couples with the plasmon. (b) Maximum amplitude oscillation of the plasmon eigenwavelength, $\Delta\lambda_{SPP\,max}$, as modulated by localized elastic mode (3) versus lattice parameter a in case of the periodic multilayer system depicted in Fig. 1(a). (c) Displacement field norm map associated with Sezawa mode (5) [seen in Fig. 1(h)] within the system depicted in Fig. 5(a). The mode is excited by placing six linear sources of force parallel to each other on top of the structure inlet (on top of polymer material); the sources are spaced by $a_x = 2\pi/k_x$, such that $k_x = 2.1877.10^6$ rad/m. Associated frequency value is $f = 0.8$ GHz [based on Fig. 1(c)]. (d) Fourier transform performed along 0-x of x component of the displacement field (u) associated with Sezawa mode (5) depicted in (b). (e) Same as (c), but for Sezawa mode (7). (f),(g) Plasmon mode eigenwavelength plotted against acoustic phase $\varphi \in [0 - pi]$ of Sezawa modes (5) and (7), respectively.

used here. Indeed, we check in the case where SiO2 replaces the polymer that $\Delta\lambda'_{SPP\,max3} \approx 4$ nm when mode (3) couples with the plasmon, which is in the same range scale as that of $\Delta\lambda_{SPP\,max3}$, although smaller. This is because mode (3) interacts with a Sezawa mode, and hence, is less localized in the pillar, resulting in a weaker coupling rate. Another dielectric material with elastic properties between those of the polymer and SiO2 materials might give rise to similar results as those obtained here.

Excitation of Sezawa surface modes (5) and (7) for the purpose of their coupling with the plasmonic mode is different due to their dispersion; indeed, at a certain frequency, one specific associated wave vector, k_x, should

be set for each mode. For instance, if we consider modes (5) and (7) at a frequency of $f = 0.8$ GHz, then associated wave vectors should be $k_x \approx 2.1877.10^6$ rad/m and $k_x = 1.4305.10^6$ rad/m, respectively, based on the system dispersion curve shown in red in Fig. 1(c). Numerically, setting of the incident surface wave k_x value is realized by placing six linear sources (of vertical force) parallel to each other on top of the structure inlet; the sources should all be set apart from each other by an amount exactly equal to $a_x = 2\pi/k_x$. In Fig. 7(c), we depict the displacement field norm map $\sqrt{|u|^2 + |v|^2 + |w|^2}$ within the structure associated with the excited Sezawa mode at $f = 0.8$ GHz and $k_x = 2.1877.10^6$ rad/m. The linear sources are highlighted by S_i, where i is $1 \leq i \leq 6$. In Fig. S4(c) within the Supplemental Material [60], we magnify part of the structure surrounding the AuNCs for comparison with the mode structure shown in Fig. 1(h) [corresponding to the periodic system of Fig. 1(c)]. Furthermore, in Fig. 7(d), we show the spatial Fourier transform, performed along the x axis, of the x component (u) of the excited mode displacement field, to check out if the associated k_x wave vector corresponds well with the correct value set (i.e., $k_x = 2.1877.10^6$ rad/m). Notably, the mode structure in Fig. 6(c) is very nearly the same as that in Fig. 1(h) and the Fourier transform of its u component is rightly centered at $k_x \approx 2.189.10^6$ rad/m, indicating successful excitation of Sezawa mode (5). Similarly, we give in Fig. S4(d) within the Supplemental Material [60] and Fig. 7(e), respectively, magnifications around AuNCs of the displacement field map within the system associated with Sezawa mode (7) ($f = 0.8$ GHz and $k_x = 1.4305.10^6$ rad/m) and the spatial Fourier transform of its u component. Here again, the observed mode structure is patently quasi-identical to the one sketched in Fig. 1(j), and Fourier transform peaks around $k_x \approx 1.4327.10^6$ rad/m, which matches the right wave vector value for mode (7) at $f = 0.8$ GHz.

The displacement field (u, v, w) associated with Sezawa modes (5) and (7) is used to deform the mesh to study phonon-plasmon coupling. The maximum elastic displacement field norm near or within gold pillars associated with the studied modes is set to be in the order of about 3 nm, as previously achieved by adjusting the strength of the force applied to the line sources. With the aim of comparing phonon-plasmon coupling strength between Sezawa and localized compressional modes, it is important that maximum displacement near or in AuNCs associated with the modes is equivalent. In that spirit, we set linear force values for Sezawa modes (5) and (7) to $F \approx 110$ and 62 N/m, respectively, which yields a maximum displacement near AuNCs of $u_{max} \approx 3$ nm for both modes. From this result, it is also notable that, for a given strength of the forces applied to line sources, the efficiency of exciting different Sezawa modes is not the same.

In Figs. 7(f) and 7(g), we report corresponding simulation results where the plasmon mode eigenwavelength

value is plotted against the Sezawa mode acoustic phases, $\varphi \in [0 - \pi]$. It can be seen that the plasmonic mode eigenwavelength is effectively modulated by Sezawa modes, such as the maximum amplitude of oscillation being $\Delta\lambda_{SPP\,max} \approx 10$ nm for mode (5) and $\Delta\lambda_{SPP\,max} \approx 19$ nm for mode (7). As observed above, concerning localized mode (3), the values of $\Delta\lambda_{SPP\,max}$ seen here are smaller than the values of this parameter taken in Figs. 4(f) and 4(g). This is related to the same reason mentioned earlier, that is, the structure only contains one unit cell along the x axis ($a \to \infty$), which results in a decrease of $\Delta\lambda_{SPP\,max}$. In fact, we depict, in Figs. S4(a) and S4(b) within the Supplemental Material [60], $\Delta\lambda_{SPP\,max}$ as a function of a for modes (5) and (7), respectively, in the periodic system of Fig. 1(a), where one notes a decrease of $\Delta\lambda_{SPP\,max}$ as a increases. Specifically, an increase of a from 1000 to 1400 nm results in $\Delta\lambda_{SPP\,max}$ decreasing by roughly 29% for mode (5) and 36.4% for mode (7), while the decrease in $\Delta\lambda_{SPP\,max}$ in Figs. 7(f) and 7(g) is about 41.2% and 44% for modes (5) and (7), respectively. The latter percentage decreases are slightly bigger than that of the former, but they correspond to the system in Fig. 5(a) for which a is infinity, indicating that the trend observed in Fig. S4(a)–S4(b) within the Supplemental Material [60] is consistent with these numbers. A comparison of the values of $\Delta\lambda_{SPP\,max}$ between different studied modes yields the following:

$$\Delta\lambda_{SPPmax} [\text{mode } (3)] \approx 19.9 \, \text{nm} \gtrsim \Delta\lambda_{SPPmax} [\text{mode } (7)]$$
$$\approx 19 \, \text{nm} > \Delta\lambda_{SPPmax} [\text{mode } (5)] \approx 10 \, \text{nm},$$

which matches roughly the same trend as that observed in Fig. 4.

To sum up, these results indicate that, for incident surface waves with amplitudes of about a few nanometers ($\sim$3 nm), which strongly overlap with the plasmon, such as Sezawa modes (5) and (7), or for those leading to excitation of localized phonons, such as mode (3), strong phonon-plasmon coupling arises, leading to the observed important plasmon frequency modulation ($\sim$20 nm). It is worth noting that comparable results have been reported in Ref. [29], where strong phonon-plasmon coupling is achieved with incident surface waves having amplitudes of about 4 nm and producing a plasmon frequency modulation up to about 14 nm.

We would like to add that tuning of plasmonic resonances is usually rather weak, but recently Maniyara *et al.* [64] were able to fabricate very thin metallic ribbons, down to 3 nm, and experimentally demonstrate a strong tuning of plasmonic resonances of the order of about 100 nm in such thin ribbons. The tuning mechanism is very different from that of our SAW-plasmon coupling, but the detuning frequencies have comparable orders of magnitude.

At last, the magnitude of plasmon frequency detuning in our work is an important fraction (or in the same scale

range) of the plasmon FWHM about 100 nm, that is, it is quite a measurable quantity, and hence, it can be employed in ultrahigh sensing applications [56]. Overall, the proposed SAW-based platform enables the achievement of strong optomechanical interactions, paving the way for various possible applications, such as ultrasensitive SAW sensors.

VI. CONCLUSION

Three-dimensional finite-element-based numerical simulations are carried out to study the surface acoustic waves interaction with localized surface plasmons in a multilayer structure supporting Au pillars. First, we study the phononic and optical properties of a periodic pillared multilayer system. Four low-frequency localized elastic modes within AuNCs are identified and three branches corresponding to Sezawa modes confined near the surface of the system are observed. The latter modes arise from of the interaction of Sezawa modes localized in the Au thick film and localized modes in AuNCs. Optical simulations reveal a strong resonance at 1543 nm, where the absorption coefficient reaches almost 64%; the resonance is shown to correspond to the so-called MIM localized surface plasmon mode. This mode is strongly confined at the bottom of AuNCs. Using a moving-mesh effect, we investigate the interaction of localized elastic and Sezawa modes with the plasmonic mode by simulating the eigenfrequency (or absorbance) of the plasmon versus the phase of acoustic modes. It is found that localized compression and Sezawa modes belonging to the upper (unfolded) branch induce a higher coupling magnitude, followed by the lower branch Sezawa modes. This is related to the localization of these modes, which is such that they compress-stretch the MIM-like cavity volume underneath AuNCs while oscillating. The surface acoustic waves interaction with the plasmon is performed in a finite multilayered system with one periodic row of AuNCs deposited on its top. SAW are excited at the structure inlet in front of the row of gold pillars and their coupling with the latter results in excitation of localized phonons in AuNCs. We show using the moving-mesh effect that the localized plasmon eigenfrequency is effectively modulated as a function of the SAW temporal phase. We uncover the role of interactions between the pillars on the phonon-plasmon coupling magnitude by showing how the latter drops as the distance between the former increases. As in the periodic multilayer system, compression and Sezawa modes of the upper (unfolded) branch induce a higher coupling rate followed by the lower branch Sezawa mode. Localized and Sezawa modes that strongly couple with the plasmon might be quite useful for an experimental realization based on the proposed geometry design, which, in turn, may greatly help the design of different nano-optomechanical devices. Additionally, owing to the sensitivity of its plasmonic response, the proposed platform can be harnessed to develop acousto-optic

devices for the detection of high-frequency acoustic waves or SAW ($\sim$GHz). Our concept is in line with previous works, such as in Ref. [65], where surface plasmon-polariton sensitivity to the immediate dielectric environment is exploited to sense acoustic waves, or in Ref. [66], where broadband detection of ultrasound is used for photoacoustic microscopy. Recently, Balram *et al*. [67] used optomechanical-based systems to conceive chip-scale acousto-optic modulation devices. On the other hand, the MIM cavity in our system, where phonons strongly overlap with localized plasmons, can be regarded as an effective optomechanical cavity, whereby acousto-optic modulation monitored by SAW can be achieved. Furthermore, based on such a cavity, various potential applications involving enhanced sound-light interaction and fast coherent acoustic control of optomechanical devices can be realized [29].

Acousto-optic devices for light modulation in the IR region specifically are still lacking, mainly due to a weak phonon-photon interaction efficiency [68]; therefore, the SAW-acoustoplasmonic platform proposed in our work, with strong phonon-plasmon coupling around 1.55 μm, may be employed to design efficient nanoscale acousto-optic light modulators in the infrared region. Finally, the proposed SAW system may be integrated into microfluidic devices, whereby SAW-driven homogeneous micromixing of multiple laminar flows results in the alteration of the refractive index near the MIM cavity [69], and hence, the frequency of the localized plasmon in the latter is modulated, which could lead, based on such an acousto-plasmofluidic device, to the design of modulators, filters, biosensors, and optical switches. Additionally, measurements by means of pump-and-probe ultrafast spectroscopy [56] would be able to detect SAW amplitudes as small as a few pm, while acoustic waves of a few pm in amplitude generated by e optical excitation can be detected by IDTs. Thus, nanoscale mechanical ultrasensitive high-frequency sensors may be envisaged based on the strong optomechanical effects achieved by our SAW system, as shown in Ref. [70].

[1] D. A. Fuhrmann, M. T. Susanna, H. kim, D. Bouwmeester, P. M. Petroff, A. Wixforth, and H. J. Krenner, Dynamic modulation of photonic crystal nanocavities using gigahertz acoustic phonons, Nat. Photonics **5,** 605 (2011).

[2] M. Metcalfe, S. M. Carr, A. Muller, G. S. Solomon, and J. Lawall, Resolved Sideband Emission of InAs/GaAs Quantum Dots Strained by Surface Acoustic Waves, Phys. Rev. Lett. **105**, 037401 (2010).

[3] V. Laude, A. Belkhir, A. F. Alabiad, M. Addouche, S. Benchabane, A. Khelif, and F. I. Baida, Extraordinary nonlinear transmission modulation in a doubly resonant acousto-optical structure, Optica **4**, 1245 (2017).

[4] S. Völk, F. J. R. Schülein, F. Knall, D. Reuter, A. D. Wieck, T. A. Truong, H. Kim, P. M. Petroff, A. Wixforth, and H. J. Krenner, Enhanced sequential carrier capture into individual quantum dots and quantum posts controlled by surface acoustic waves, Nano Lett. **10**, 3399 (2010).

[5] T. Berstermann, C. Brüggemann, M. Bombeck, A. V. Akimov, D. R. Yakovlev, C. Kruse, D. Hommel, and M. Bayer, Optical bandpass switching by modulating a microcavity using ultrafast acoustics, Phys. Rev. B **81**, 085316 (2010).

[6] T. J. Kippenberg and K. J. Vahala, Cavity optomechanics: Back-action at the mesoscale, Science **321**, 1172 (2008).

[7] I. Favero and K. Karrai, Optomechanics of deformable optical cavities, Nat. Photon. **3**, 201 (2009).

[8] W. Aspelmeyer, T. J. Kippenberg, and F. Marquardt, Cavity optomechanics, Rev. Mod. Phys. **86**, 1391 (2014).

[9] M. Aspelmeyer, P. Meystre, and K. Schwab, Quantum optomechanics, Phys. Today **65**, 29 (2012).

[10] E. Gil-Santos, C. Baker, D. T. Nguyen, W. Hease, C. Gomez, A. Lemaître, S. Ducci, G. Leo, and I. Favero, High-frequency nano-optomechanical disk resonators in liquids, Nat. Nanotechnol. **10**, 810 (2015).

[11] D. Royer and E. Dieulesaint, *Elastic Waves in Solids* (Springer, New York, 2000).

[12] A. Yariv and P. Yeh, *Optical Waves in Crystals* (John Wiley and Sons, New Jersey, 2003).

[13] I. E. Psarobas, N. Papanikolaou, N. Stefanou, B. Djafari-Rouhani, B. Bonello, and V. Laude, Enhanced acousto-optic interactions in a one-dimensional phoxonic cavity, Phys. Rev. B **82**, 174303 (2010).

[14] M. Maldovan, Sound and heat revolutions in phononics, Nature **503**, 209 (2013).

[15] Q. Rolland, M. Oudich, S. El-Jallal, S. Dupont, Y. Pennec, J. Gazalet, J. C. Kastelik, G. Lévêque, and B. Djafari-Rouhani, Acousto-optic couplings in two-dimensional phoxonic crystal cavities, Appl. Phys. Lett. **101**, 061109 (2012).

[16] S. Eljallal, M. Oudich, Y. Pennec, B. Djafari-Rouhani, A. Makhoute, Q. Rolland, S. Dupont, and J. Gazalet, Optomechanical interactions in two-dimensional Si and GaAs phoXonic cavities, J. Phys.: Condensed Matter **26**, 015005 (2014).

[17] M. Eichenfield, J. Chan, R. M. Camacho, K. J. Vahala, and O. Painter, Optomechanical crystals, Nature **462**, 78 (2009).

[18] M. Eichenfield, J. Chan, A. H. Safavi-Naeini, K. J. Vahala, and O. Painter, Modeling dispersive coupling and losses of localized optical and mechanical modes in optomechanical crystals, Opt. Express **17**, 20078 (2009).

[19] J. Chan, A. H. Safavi-Naeini, J. T. Hill, S. Meenehan, and O. Painter, Optimized optomechanical crystal cavity with acoustic radiation shield, Appl. Phys. Lett. **101**, 081115 (2012).

[20] M. Oudich, S. El-Jallal, Y. Pennec, B. Djafari-Rouhani, J. Gomis-Bresco, D. Navarro-Urrios, C. M. Sotomayor Torres, A. Martınez, and A. Makhoute, Optomechanic interaction in a corrugated phoxonic nanobeam cavity, Phys. Rev. B **89**, 245122 (2014).

[21] J. Gomis-Bresco, D. Navarro-Urrios, M. Oudich, S. El-Jallal, A. Griol, D. Puerto, E. Chavez, Y. Pennec, B. Djafari-Rouhani, F. Alzina, A. Martınez, and C. M. Sotomayor Torres, A one-dimensional optomechanical crystal with a complete phononic band gap, Nat. Commun. **5**, 4452 (2014).

[22] B. Djafari-Rouhani, S. El-Jallal, and Y. Pennec, Phoxonic crystals and cavity optomechanics, C. R. Physique **17**, 555 (2015).

[23] E. Gavartin, R. Braive, I. Sagnes, O. Arcizet, A. Beveratos, and T. J. Kippenberg, Optomechanical Coupling in a Two-Dimensional Photonic Crystal Defect Cavity, Phys. Rev. Lett. **106**, 203902 (2011).

[24] Y. G. Roh, T. Tanabe, A. Shinya, H. Taniyama, E. Kuramochi, S. Matsuo, T. Sato, and M. Notomi, Strong optomechanical interaction in a bilayer photonic crystal, Phys. Rev. B **81**, 121101 (2010).

[25] A. H. Safavi-Naeini and O. Painter, Design of optomechanical cavities and waveguides on a simultaneous bandgap phononic-photonic crystal slab, Opt. Express **18**, 14926 (2010).

[26] M. H. Aram and S. Khorasani, Optomechanical coupling strength in various triangular phoxonic crystal slab cavities, J. Opt. Soc. Am. B **35**, 1390 (2018).

[27] J.-C. Hsu, J.-H. Shih, and T.-R. Lin, Deep-subwavelength plasmonic-photonic hybrid band gap opening by acoustic Lamb waves, Appl. Phys. Lett. **111**, 021904 (2017).

[28] T.-R. Lin, Y.-C. Huang, and J.-C. Hsu, Optomechanical coupling in phoxonic–plasmonic slab cavities with periodic metal strips, J. Appl. Phys. **117**, 173105 (2015).

[29] T.-R. Lin, C.-H. Lin, and J.-C. Hsu, Strong optomechanical interaction in hybrid plasmonic-photonic crystal nanocavities with surface acoustic waves, Sci. Rep. **5**, 13782 (2015).

[30] P. K. Parashar and V. K. Komarala, Engineered optical properties of silver-aluminum alloy nanoparticles embedded in SiON matrix for maximizing light confinement in plasmonic silicon solar cells, Sci. Rep. **7**, 12520 (2017).

[31] E. Palacios, A. Chen, J. Foley, S. K. Gray, U. Welp, D. Rosenmann, and V. K. Vlasko-Vlasov, Ultra-confined modes in metal nanoparticle arrays for subwavelength light guiding and amplification, Adv. Optical Mater. **2**, 394 (2014).

[32] G. Z. Gaydan, O. M. Demkiv, N. Ye. Stasyuk, R. Y. Serkiz, M. D. Lootsik, A. Errachid, M. V. Gonchar, and M. Nisnevitch, Metallic nanoparticles obtained via "green" synthesis as a platform for biosensor construction, Appl. Sci. **9**, 720 (2019).

[33] F. Fathi, M. R. Rashidi, and Y. Omidi, Ultra-sensitive detection by metal nanoparticles-mediated enhanced SPR biosensors, Talanta **192**, 118 (2019).

[34] R. Salahandish, A. Ghaffarinejad, S. M. Naghib, A. Niyazi, K. Majidzadeh-A, M. Janmaleki, and Amir Sanati-Nezhad, Sandwich-structured nanoparticles-grafted functionalized graphene based 3D nanocomposites for high-performance biosensors to detect ascorbic acid biomolecule, Sci. Rep. **9**, 1226 (2019).

[35] M. Kim, J.-H. Lee, and J.-M. Nam, Plasmonic photothermal nanoparticles for biomedical application, Adv. Sci. **6,** 1900471 (2019).

[36] M. R. K. Ali, Y. Wu, and M. A. El-Sayed, Gold-nanoparticle-assisted plasmonic photothermal therapy advances toward clinical application, J. Phys. Chem. C **123,** 15375 (2019).

[37] K. Kluczyk, C. David, J. Jacak, and W. Jacak, On modeling of plasmon-induced enhancement of the efficiency of solar cells modified by metallic nano-particles, Nanomaterials **9,** 3 (2019).

[38] G. Singh and S. S. Verma, Plasmon enhanced light trapping in thin film GaAs solar cells by Al nanoparticle array, Phys. Lett. A **383,** 1526 (2019).

[39] M. A. van Dijk, M. Lippitz, and M. Orrit, Detection of Acoustic Oscillations of Single Gold Nanospheres by Time-Resolved Interferometry, Phys. Rev. Lett. **95,** 267406 (2005).

[40] H. Staleva and G. V. Hartland, Vibrational dynamics of silver nanocubes and nanowires studied by single-particle transient absorption spectroscopy, Adv. Funct. Mater. **18,** 3809 (2008).

[41] M. Hu, X. Wang, G. V. Hartland, P. Mulvaney, J. P. Juste, and J. E. Sader, Vibrational response of nanorods to ultrafast laser induced heating: theoretical and experimental analysis, J. Am. Chem. Soc. **125,** 14925 (2003).

[42] N. Large, L. Saviot, J. Margueritat, J. Gonzalo, C. N. Afonso, A. Arbouet, P. Langot, A. Mlayah, and J. Aizpurua, Acousto-plasmonic Hot spots in metallic nano-objects, Nano Lett. **9,** 3732 (2009).

[43] F. Della Picca, R. Berte, M. Rahmani, P. Albella, J. M. Bujjamer, M. Poblet, E. Cortés, S. A. Maier, and A. V. Bragas, Tailored hypersound generation in single plasmonic nanoantennas, Nano Lett. **16,** 1428 (2016).

[44] C. Voisin, N. Del Fatti, D. Christofilos, and F. Vallee, Time-resolved investigation of the vibrational dynamics of metal nanoparticles, Appl. Surf. Sci. **164,** 131 (2000).

[45] A. Nelet, A. Crut, A. Arbouet, N. Del Fatti, F. Vallee, H. Portales, L. Saviot, and E. Duval, Acoustic vibrations of metal nanoparticles: High order radial mode detection, Appl. Surf. Sci. **226,** 209 (2004).

[46] G. Bachelier, J. Butet, I. Russier-Antoine, C. Jonin, E. Benichou, and P. F. Brevet, Origin of optical second-harmonic generation in spherical gold nanoparticles: Local surface and nonlocal bulk contributions, Phys. Rev. B **82,** 235403 (2010).

[47] H. Portales, N. Goubet, L. Saviot, S. Adichtchev, D. B. Murray, A. Mermet, E. Duval, and M. P. Pileni, Probing atomic ordering and multiple twinning in metal nanocrystals through their vibrations, Proc. Natl. Acad. Sci. **105,** 14784 (2008).

[48] S. Tripathy, R. Marty, V. Kaixin Lin, S. Lang Teo, E. Ye, A. Arbouet, L. Saviot, C. Girard, M. Yong Han, and A. Mlayah, Acousto-plasmonic and surface-enhanced Raman scattering properties of coupled gold nanospheres/nanodisk trimers, Nano Lett. **11,** 431 (2011).

[49] A. Mrabti, G. Lévêque, A. Akjouj, Y. Pennec, B. Djafari-Rouhani, R. Nicolas, T. Maurer, and P. M. Adam, Elasto-plasmonic interaction in metal-insulator-metal localized surface plasmon systems, Phys. Rev. B **94,** 075405 (2016).

[50] K. C. Balram, M. I. Davanço, J. D. Song, and K. Srinivasan, Coherent coupling between radiofrequency, optical and acoustic waves in piezo-optomechanical circuits, Nat. Photon. **10,** 346 (2016).

[51] H. Li, S. A. Tadesse, Q. Liu, and M. Li, Nanophotonic cavity optomechanics with propagating acoustic waves at frequencies up to 12GHz, Optica **2,** 826 (2015).

[52] A. Vainsencher, K. J. Satzinger, G. A. Peairs, and A. N. Cleland, Bi-directional conversion between microwave and optical frequencies in a piezoelectric optomechanical device, Appl. Phys. Lett. **109,** 033107 (2016).

[53] M. Hu and F. L. Duan, Design, fabrication and characterization of SAW devices on LiNbO3 bulk and ZnO thin film substrates, Solid State Electron. **150,** 28 (2018).

[54] R. Salenbien, R. Côte, J. Goossens, P. Limaye, R. Labie, and C. Glorieux, Laser-based surface acoustic wave dispersion spectroscopy for extraction of thicknesses, depth, and elastic parameters of a subsurface layer: Feasibility study on intermetallic layer structure in integrated circuit solder joint, J. Appl. Phys. **109,** 093104 (2011).

[55] A. Crut, P. Maioli, N. Del Fatti, and F. Vallée, Acoustic vibrations of metal nano-objects: Time-domain investigations, Phys. Rep. **549,** 1 (2015).

[56] G. Soavi, I. Tempra, M. F. Pantano, A. Cattoni, S. Collin, P. Biagioni, N. M. Pugno, and G. Cerullo, Ultrasensitive characterization of mechanical oscillations and plasmon energy shift in gold nanorods, ACS Nano **10,** 2251 (2016).

[57] C. Yi, P. D. Dongare, M.-N. Su, W. Wang, D. Chakraborty, F. Wen, W.-S. Chang, J. E. Sader, P. Nordlander, N. J. Halas, and S. Link, Vibrational coupling in plasmonic molecules, PNAS **114,** 11621 (2017).

[58] Z. Wang, Q. Wang, W. Zhang, H. Wei, Y. Li, and W. Ren, Ultrasensitive photoacoustic detection in a high-finesse cavity with pound–drever–hall locking, Opt. Lett. **44,** 1924 (2019).

[59] P. J. M. van der Slot, M. A. G. Porcel, and K. J. Boller, Surface acoustic waves for acousto-optic modulation in buried silicon nitride waveguides, Opt. Express **27,** 1433 (2019).

[60] See the Supplemental Material at http://link.aps.org/supplemental/10.1103/PhysRevApplied.13.024077 for further simulation data and details of the numerical method concerning the search for localized plasmons modes of the pillared multilayer structure.

[61] Y. Jin, B. Bonello, R. P. Moiseyenko, Y. Pennec, O. Boyko, and B. Djafari-Rouhani, Pillar-type acoustic metasurface, Phys. Rev. B **96,** 104311 (2017).

[62] A. V. Korovin, Y. Pennec, M. Stocchi, D. Mencarelli, L. Pierantoni, T. Makkonen, J. Ahopelto, and B. Djafari-Rouhani, Conversion between surface acoustic waves and guided modes of a quasi-periodic structured nanobeam, J. Phys. D: Appl. Phys. **52,** 32LT01 (2019).

[63] G. Chow, E. Uchaker, G. Cao, and J. Wang, Laser-induced surface acoustic waves: An alternative method to nanoindentation for the mechanical characterization of porous nanostructured thin film electrode media, Mech. Mater. **91,** 333 (2015).

[64] R. A. Maniyara, D. Rodrigo, R. Yu, Josep Canet-Ferrer, D. S. Ghosh, R. Yongsunthon, D. E. Baker, A. Rezikyan,

F. J. García de Abajo, and V. Pruneri, Tunable plasmons in ultrathin metal films, Nat. Photonics **13**, 328 (2019).

[65] A. A. Kolomenskii, E. Surovic, and H. A. Schuessler, Optical detection of acoustic waves with surface plasmons, Appl. Opt. **57**, 5604 (2018).

[66] T. Wang, R. Cao, B. Ning, A. J. Dixon, J. A. Hossack, A. L. Klibanov, Q. Zhou, A. Wang, and S. Hu, All-optical photoacoustic microscopy based on plasmonic detection of broadband ultrasound, Appl. Phys. Lett. **107**, 153702 (2015).

[67] K. C. Balram, M. I. Davanço, B. R. Ilic, J.-H. Kyhm, J. D. Song, and K. Srinivasan, Acousto-Optic Modulation and Optoacoustic Gating in Piezo-Optomechanical Circuits, Phys. Rev. Appl. **7**, 024008 (2017).

[68] I. M. Sopko and G. A. Knyazev, Optical modulator based on acousto-plasmonic coupling, Phys. Wave Phenom **24**, 124 (2016).

[69] D. Ahmed, X. Peng, A. Ozcelik, Y. Zheng, and T. J. Huang, Acousto-plasmofluidics: Acoustic modulation of surface plasmon resonance in microfluidic systems, AIP Adv. **5**, 097161 (2015).

[70] M. Li, H. X. Tang, and M. L. Roukes, Ultra-sensitive NEMS-based cantilevers for sensing, scanned probe and very high-frequency applications, Nat. Nanotechnol. **2**, 114 (2007).